Simultaneous Measurement of Microwave Doppler Frequency Shift and Angle of Arrival Based on a Silicon Integrated Chip

Liangzun Tang, Zhenzhou Tang, *Member, IEEE*, Simin Li, Shifeng Liu, and Shilong Pan, *Senior Member, IEEE, Fellow, OPTICA*

***Abstract*—A system for simultaneous measurement of microwave Doppler-frequency-shift (DFS) and angle-of-arrival (AOA) is proposed based on a silicon integrated chip. In the chip, two dual-drive Mach-Zehnder modulators (DDMZMs) with a micro-ring resonator (MRR) inserted between them are integrated. When an external laser is coupled into the chip, it is firstly modulated by two echo signals via the first DDMZM, and then goes through the MRR to introduce an optical phase shift to one of the first-order sidebands that falls into the resonance of the MRR. After being re-modulated by the transmitted signal at the other DDMZM, the lightwave is coupled out from the chip and separated into two channels by an optical coupler. In each channel, a band-pass filter (BPF) is employed to select the upper and lower sidebands, respectively. By measuring and comparing the powers, frequencies, and phases of the beat signals in the two channels, the DFS (without direction ambiguity) and AOA can be acquired. Based on the proposed method, DFS within ± 100 kHz at 10, 15, and 20 GHz is successfully estimated with a maximum error of ±0.028 Hz, and AOA measurement from 0° to 75° with errors less than ±1.53° is also realized.**

***Index Terms*—DFS and AOA measurement, microwave photonics, integrated photonics, silicon-on-insulator.**

I. Introduction

MEASUREMENT of Doppler frequency shift (DFS) and angle of arrival (AOA) of a microwave signal is essential in numerous applications, including electronic warfare [1], self-driving vehicles [2], and radar systems [3]-[5], since the DFS and AOA can derive the radial velocity and direction of the moving target relative to the antennas array. Nowadays, due to the diverse application scenarios and complex electromagnetic environment, most of the measurement systems are facing the challenges of limited bandwidth, high power consumption, and severe electromagnetic interference, which are difficult to overcome by traditional electrical methods because of the electrical bottlenecks. Under this background, the photonic measurement schemes [6]-[8], with advantages of wide bandwidth, light weight, and immunity to electromagnetic interference, are regarded as a potential solution.

In general, the photonic AOA estimation methods can be divided into two categories. In the first category, the AOA information is obtained by measuring the relative time delay between the received signals [9]-[11]. To do so, a tunable transversal microwave photonic notch filter (MPF) is usually built, and the relative time delay is mapped to the frequency of the notch [9], [10] or the power of the filtered electrical signals [11]. Although this kind of AOA measurement system has a wide bandwidth (since no optical filter is employed), the AOA measurement range is usually limited and high-speed photodetectors (PDs) are also required. Methods in the second category are implemented based on the calculation of the phase difference between the echo signals [12]-[17]. In this category, optical interference is mainly utilized to extract the phase difference. For example, through the interference of modulated optical sidebands, the output optical power [12]-[14], DC voltage [15], or electrical power [16], [17] would be changed. Thus, the phase difference can be easily acquired by utilizing cheap optical or electrical power meters to monitor these parameters.

As for the measurement of the microwave DFS, the absolute value can be easily acquired by frequency mixing between the transmitted signal and echo signal, so the main attention is always paid to distinguishing the direction of the DFS. For this reason, two main kinds of photonic methods for DFS measurement with direction discrimination are proposed [18]-[29]. The first kind is realized by extracting and comparing the phase relationship of the intermediate frequency (IF) signal obtained by frequency mixings between the echo signals with the transmitted signals in two different channels [18]-[22]. The key point, in this method, is to introduce a phase difference between the two IF signals. However, most of the phase differences are introduced by complex modulations, which makes the systems sensitive to the bias point and the polarization state. Although a passive dispersion medium can also be used to introduce the phase shift [19], long fiber is required to provide a sufficient phase difference, making the

Manuscript xxxx. This work was supported in part by National Key R&D Program of China (2018YFB2201803, 2020YFB1805704), the National Natural Science Foundation of China under Grants 62001218, and the National Natural Science Foundation of Jiangsu Province under Grant BK20200436. (Corresponding author: *Zhenzhou Tang, Shilong Pan*.)

The authors are with the Key Laboratory of Radar Imaging and Microwave Photonics, Ministry of Education, Nanjing University of Aeronautics and Astronautics, Nanjing 210016, China (e-mail: lztang@nuaa.edu.cn; tangzhzh@nuaa.edu.cn; lisimin@nuaa.edu.cn; sfliu_nuaa@nuaa.edu.cn; pans@ieee.org).

system bulky and hard to be integrated. Unlike the first kind that is based on phase comparison, the second kind of method is implemented by measuring the relative frequency relationship of the down-converted IF signals in the electrical spectrum analyzer (ESA). Since an additional reference signal [26]-[29] or an optical frequency shift module [23]-[25] is needed, the system cost will be increased.

Another special kind of DFS measurement method based on a class of Doppler frequency estimation (DFE) system have also been proposed [30]-[32]. The DFS information is extracted by utilizing the four-wave mixing effect in a highly nonlinear fiber instead of microwave frequency mixing. The operating carrier frequency of this system could be as high as 40 GHz without using high-cost devices and high-measurement sensitivity also could be achieved by utilizing a lock-in amplification technique [32].

The aforementioned schemes can only measure DFS or AOA separately, but in most situations, both the direction and velocity of the target need to be obtained. Recently, several photonic approaches have been published [2], [33]-[36] to measure the DFS and AOA simultaneously. However, since these multi-functional systems are promoted from the previous single-functional systems, they still have similar problems in terms of complex modulation, complicated structure, additional reference source, etc. More importantly, these systems are all built by discrete devices, which suffer from the inherent disadvantages of bulky size, high cost, high power consumption, and instability. Therefore, a high degree of system integration is desirable. For example, a silicon integrated chip is used to measure the DFS [37], but this scheme needs an additional reference source and it cannot measure the AOA.

In this paper, we propose a DFS and AOA measurement system based on a silicon integrated chip. The chip, fabricated in the silicon-on-insulator (SOI) platform, consists of two dual-drive Mach-Zehnder modulators (DDMZMs) and a micro-ring resonator (MRR) inserted between the two DDMZMs. In the proposed measurement system, an external light is coupled into the chip and modulated by two received signals at the first DDMZM, and then goes through the MRR to introduce an optical phase shift to one of the first-order sidebands that falls into the resonance of the MRR. After being re-modulated by the transmitted signal at the other DDMZM, the lightwave is coupled out from the chip and separated into two channels. In each channel, a band-pass filter (BPF) is employed to select the upper and lower sidebands, respectively. By measuring and comparing the powers, frequencies, and phases of the beat signals generated by low-speed photodetectors (PDs) connected to the two channels, both the DFS (without direction ambiguity) and AOA can be obtained. As compared with the previous approaches, the proposed system has the following advantages: 1) This structure does not require an additional reference source or frequency shift module. The phase shift module in our work is an integrated passive device (i.e., the MRR), which can be easily controlled by a DC source. 2) No complex modulation, precise bias control, or polarization-division-multiplexed I/Q detection is required in the proposed structure. The modulators in our system are naturally biased near the maximum transmission point owing to the almost identical length of the two branches, so the system complexity can be significantly reduced. 3) Since most of the devices are integrated on a single chip, it has the advantages of small size, light weight, low cost, and low power consumption. Even though this structure is not a fully-integrated system, it still provides a feasible way towards the high-performance monolithic integration of AOA and DFS measurement system.

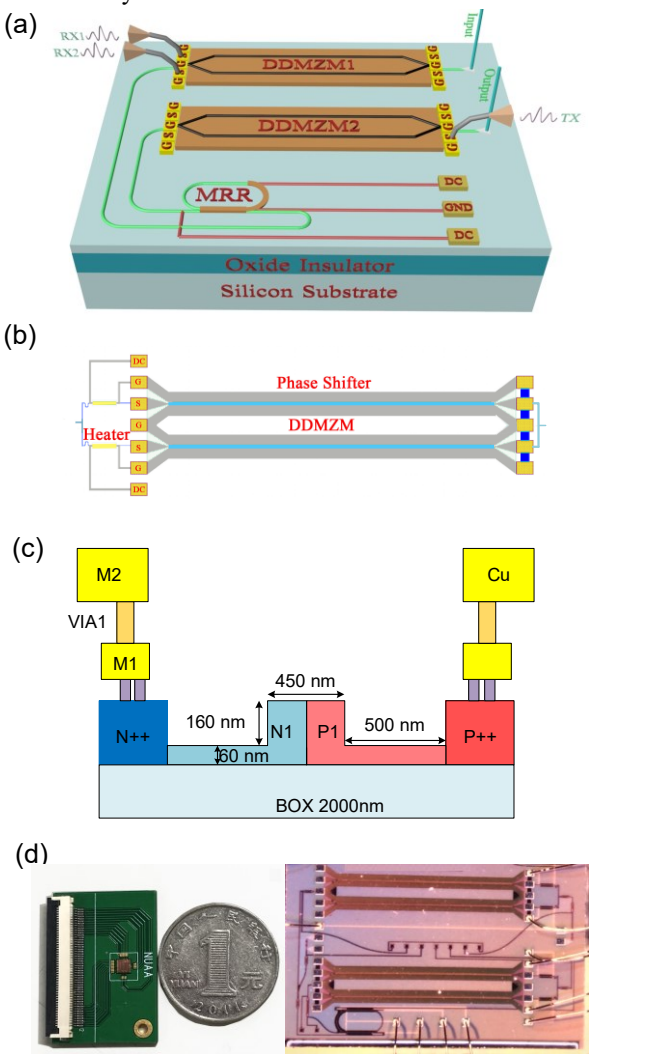

Fig. 1. (a) Schematic diagram of the chip. (b) Configuration of the modulator. (c) Cross-section of the phase shifter. (d) The picture and zoom-in view of the chip. M1: Cu metal 1, M2: Cu metal 2, VIA: Via between M1 and M2, DDMZM: dual-drive Mach-Zehnder modulator, MRR: micro-ring resonator, DC: direct current.

II. Device Design and Characterization

As can be seen from the schematic diagram in Fig. 1(a), two DDMZMs and an MRR are fabricated on the 220-nm SOI chip by a multi-project-wafer (MPW) service provided by Interuniversity Microelectronics Centre (IMEC), Leuven, Belgium. As shown in Fig. 1(b), the DDMZMs employ a balanced traveling-wave Mach-Zehnder interference structure with a phase shifter and a heater in each arm. The cross-section

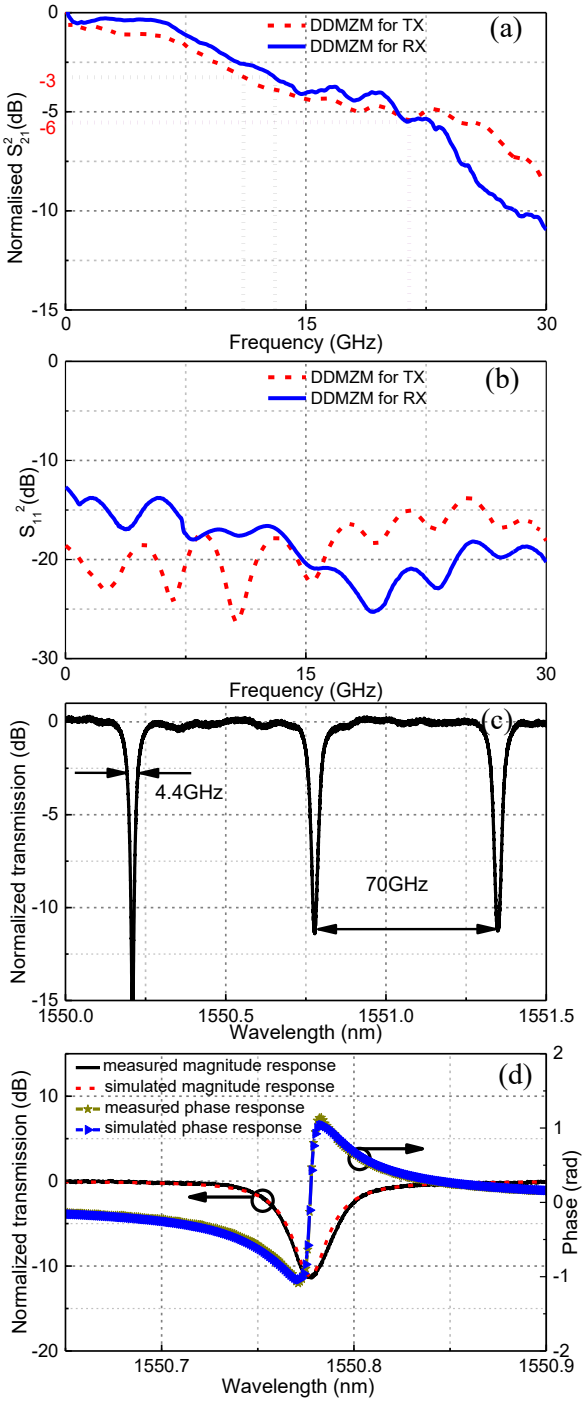

Fig. 2. (a) S_{21} and (b) S_{11} of the on-chip modulators. (c) Normalized transmission of the micro-ring resonator. (d) Measured and simulated transmission response of the resonance employed in the experiment. RX: the received signal, TX: the transmitted signal.

of the phase shifter is depicted in Fig. 1(c) and some parameters are annotated in it. At the input and output ports of the DDMZMs, two multi-mode interferometers (1×2 and 2×1) with ~3 dB transmission loss are employed. An MRR based on a racetrack ring structure with lateral coupling is inserted between the two DDMZMs. The length of the racetrack is 200 μm and the diameter of the semicircle is 190 μm. Two TE mode grating couplers are used to couple the light into and out of the chip. Fig. 1(d) shows the picture and zoom-in view of the chip. The size of the chip is as small as 1.45 mm×2.5 mm and the DC pads used to tune the resonance of the MRR and the bias points of the DDMZMs are packaged on a printed circuit board.

The performances of the DDMZMs and the MRR are firstly measured by a high-resolution optical vector analyzer (Newkey Photonics GOCA-67). The fiber-to-fiber loss (including the coupling loss) of the whole chip is about 34 dB. As can be seen from the S_{21} curve of the DDMZM shown in Fig. 2(a), the 3-dB (6-dB) bandwidths of the two modulators are 11.1 GHz (21.4 GHz) and 13.1 GHz (21.4 GHz), respectively. Fig. 2(b) also presents the measured S_{11} of the DDMZMs. Since the S_{11} values are all below -12.5 dB, a good impedance matching is achieved. In addition, from Fig. 2(c), the 3-dB bandwidth of the MRR is about 4.4 GHz and the free spectrum range (FSR) is about 70 GHz. The measured and simulated transmission responses of the MRR are shown in Fig. 2(d). The measured results are in good agreement with the simulation results, and the maximum phase shift in the resonance region exceeds 1 radian (about 57.3°).

III. Principle

The schematic diagram of the proposed system based on the silicon integrated chip is depicted in Fig. 3. An external optical carrier is amplified by an erbium-doped fiber amplifier (EDFA1) and launched into the first DDMZM (DDMZM1) on the chip. A polarization controller (PC) is used to tune the polarization state of the optical carrier. Two echo signals received by two antennas with a phase difference of θ are applied to the two branches of DDMZM1. Assuming that the distance between the antennas is $\lambda/2$ (i.e., $d=\lambda/2$, where λ is the wavelength of the transmitted signal) [38], the relationship between AOA and the phase difference can be expressed as $\psi=\arcsin(\theta/\pi)$. The bias of DDMZM1 is naturally set near the maximum transmission point, so the output signal of DDMZM1 can be given by

$$E_{out1}(t)=\sqrt{\frac{t_{ff}}{2}}E_0\exp(j\omega_c t)\left[\begin{array}{l}\exp(j\beta_e\cos\omega_e t)\\+\exp\left(j\beta_e\cos\left(\omega_e t+\theta\right)\right)\end{array}\right] \quad (1)$$

where E_0 and ω_c are the amplitude and angular frequency of the optical carrier, ω_e is the angular frequency of the echo signals, t_{ff} is the optical loss (including the coupling loss of the input port and the insertion loss of DDMZM1), β_e is the modulation index which is defined by $\beta_e=\pi V_0/2V_\pi$, where V_0 and V_π are the amplitude voltages of the echo signal and the half-wave voltage of the modulator, respectively. When ignoring the high-order sidebands, (1) can be expanded as

$$E_{out1}(t)=\sqrt{\frac{t_{ff}}{2}}E_0\left\{\begin{array}{l}2J_0(\beta_e)\exp(j\omega_c t)\\+\sqrt{2(1+\cos\theta)}J_1(\beta_e)\exp\left\{j\left[(\omega_c-\omega_e)t-\frac{\theta-\pi}{2}\right]\right\}\\+\sqrt{2(1+\cos\theta)}J_1(\beta_e)\exp\left\{j\left[(\omega_c+\omega_e)t+\frac{\theta+\pi}{2}\right]\right\}\end{array}\right\} \quad (2)$$

The optical spectrum at the output of DDMZM1 is illustrated in Fig. 3(a). When the modulated signal goes through the MRR and the wavelength of the optical carrier is adjusted to make the -1st-order sideband fall in the resonance region of the MRR, a

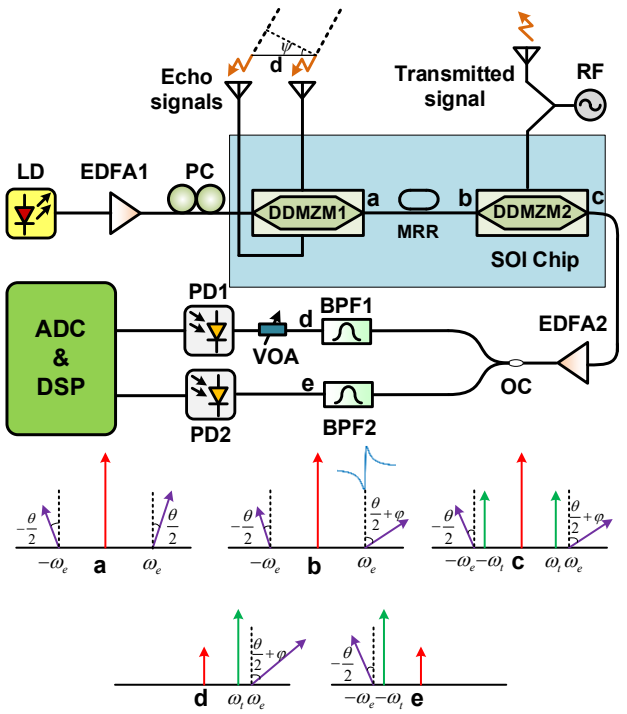

Fig. 3. The proposed DFS and AOA measurement system and the optical spectra at different locations. DDMZM: dual-drive Mach–Zehnder modulator, PC: polarization controller, LD: laser diode, EDFA: erbium-doped fiber amplifier, MRR: micro-ring resonator, RF: radio frequency, OC: optical coupler, BPF: bandpass filter, PD: photodetector.

non-zero phase shift φ is introduced to this sideband, as shown in Fig. 3(b). Then, the output signal of the MRR is re-modulated by the transmitted signal at the other DDMZM (DDMZM2), and the output can be written as

$$E_{out2}(t)=\frac{\sqrt{t_{ff}\cdot t_{fs}}}{2}\left\{\begin{array}{l}2J_0(\beta_e)\exp(j\omega_c t)\\ +\sqrt{t_{fr}}\cdot\sqrt{2(1+\cos\theta)}J_1(\beta_e)\exp\left\{j\left[(\omega_c-\omega_e)t-\frac{\theta-\pi}{2}+\varphi\right]\right\}\\ +\sqrt{2(1+\cos\theta)}J_1(\beta_e)\exp\left\{j\left[(\omega_c+\omega_e)t+\frac{\theta+\pi}{2}\right]\right\}\end{array}\right\}\times\left[1+\exp(j\beta_t\cos\omega_t t)\right] \quad (3)$$

where ω_t is the angular frequency of the transmitted signal, t_{fs} and t_{fr} are the optical losses (including the coupling loss of the output port and the insertion loss of DDMZM2) and the extra loss induced by the MRR, β_t is the modulation index. By using the Jacobi–Anger expansion again, (3) can be further written as

$$E_{out2}(t)=\frac{\sqrt{t_{ff}\cdot t_{fs}}}{2}E_0\times\left\{\begin{array}{l}2J_0(\beta_e)\left[1+J_0(\beta_t)\right]\exp(j\omega_c t)\\ +\sqrt{t_{fr}}\cdot\sqrt{2(1+\cos\theta)}J_1(\beta_e)\exp\left(j\left[(\omega_c-\omega_e)t-\frac{\theta-\pi}{2}+\varphi\right]\right)\\ +\sqrt{2(1+\cos\theta)}J_1(\beta_e)\exp\left(\left[(\omega_c+\omega_e)t+\frac{\theta+\pi}{2}\right]\right)\\ +2J_0(\beta_e)J_1(\beta_t)\exp\left(j\left[(\omega_c-\omega_t)t-\frac{\pi}{2}\right]\right)\\ +2J_0(\beta_e)J_1(\beta_t)\exp\left(j\left[(\omega_c+\omega_t)t+\frac{\pi}{2}\right]\right)\end{array}\right\} \quad (4)$$

The illustration of the optical spectrum at the output of DDMZM2 is shown in Fig. 3(c). Then, the optical signal is coupled out from the chip, and split into two channels by a 3-dB optical coupler. In each path, two adjacent sidebands are separately selected by the optical BPFs and sent to the low-speed PDs afterwards, as shown in Fig. 3(d) and Fig. 3(e). Thus, the output electrical signals (ignoring the DC components) can be written as

when $\omega_e<\omega_t$, DFS<0

$$\left\{\begin{array}{l}I_{upper}=\frac{t_{ff}\cdot t_{fs}}{2}\Re E_0^2\sqrt{2(1+\cos\theta)}\\ \quad\cdot J_0(\beta_e)J_1(\beta_t)J_1(\beta_e)\cos\left[(\omega_t-\omega_e)t-\frac{\theta}{2}\right]\\ I_{lower}=\frac{t_{ff}\cdot t_{fs}}{2}\sqrt{t_{fr}}\Re E_0^2\sqrt{2(1+\cos\theta)}\\ \quad\cdot J_0(\beta_e)J_1(\beta_t)J_1(\beta_e)\cos\left[(\omega_t-\omega_e)t-\frac{\theta}{2}+\varphi\right]\end{array}\right. \quad (5a)$$

or

when $\omega_e>\omega_t$, DFS>0

$$\left\{\begin{array}{l}I_{upper}=\frac{t_{ff}\cdot t_{fs}}{2}\Re E_0^2\sqrt{2(1+\cos\theta)}\\ \quad\cdot J_0(\beta_e)J_1(\beta_t)J_1(\beta_e)\cos\left[(\omega_e-\omega_t)t+\frac{\theta}{2}\right]\\ I_{lower}=\frac{t_{ff}\cdot t_{fs}}{2}\sqrt{t_{fr}}\Re E_0^2\sqrt{2(1+\cos\theta)}\\ \quad\cdot J_0(\beta_e)J_1(\beta_t)J_1(\beta_e)\cos\left[(\omega_e-\omega_t)t+\frac{\theta}{2}-\varphi\right]\end{array}\right. \quad (5b)$$

where $\Re$ is the responsivity of the low-speed PDs. Furthermore, the power of the electrical signals can be written as

$$\left\{\begin{array}{l}P_{upper}=\frac{t_{ff}^2\cdot t_{fs}^2}{4}\Re^2E_0^4J_0^2(\beta_e)J_1^2(\beta_t)J_1^2(\beta_e)(1+\cos\theta)\\ P_{lower}=\frac{t_{ff}^2\cdot t_{fs}^2}{2}t_{fr}\Re^2E_0^4J_0^2(\beta_e)J_1^2(\beta_t)J_1^2(\beta_e)(1+\cos\theta)\end{array}\right. \quad (6)$$

As can be seen from (5), the DFS value can be acquired by measuring the frequency of the electrical signal and the DFS direction can be known by comparing the phase difference. Besides, since the electrical power of the signals is sensitive to the phase difference, the AOA can also be acquired by measuring the electrical power as shown in (6).

Two things should be noted: 1) In (2), since the power of the sidebands is much lower than that of the optical carrier, after remodulation, the new optical components with the frequency of $\omega_c\pm\omega_e\pm\omega_t$ are relatively weak. Furthermore, these components are close to the optical carrier, so they can be easily removed after the optical bandpass filtering. Therefore, only the components with the frequencies of $\omega_c\pm\omega_t$ are considered in (3). 2) An optical variable attenuator (OVA) is adopted in the upper channel to balance the electrical power of the two channels, as shown in Fig. 3.

IV. Experimental Setup and Results

In the experiment, a 1 dBm optical carrier centered at 1552.55 nm is generated by a tunable laser source (PS-TNL,

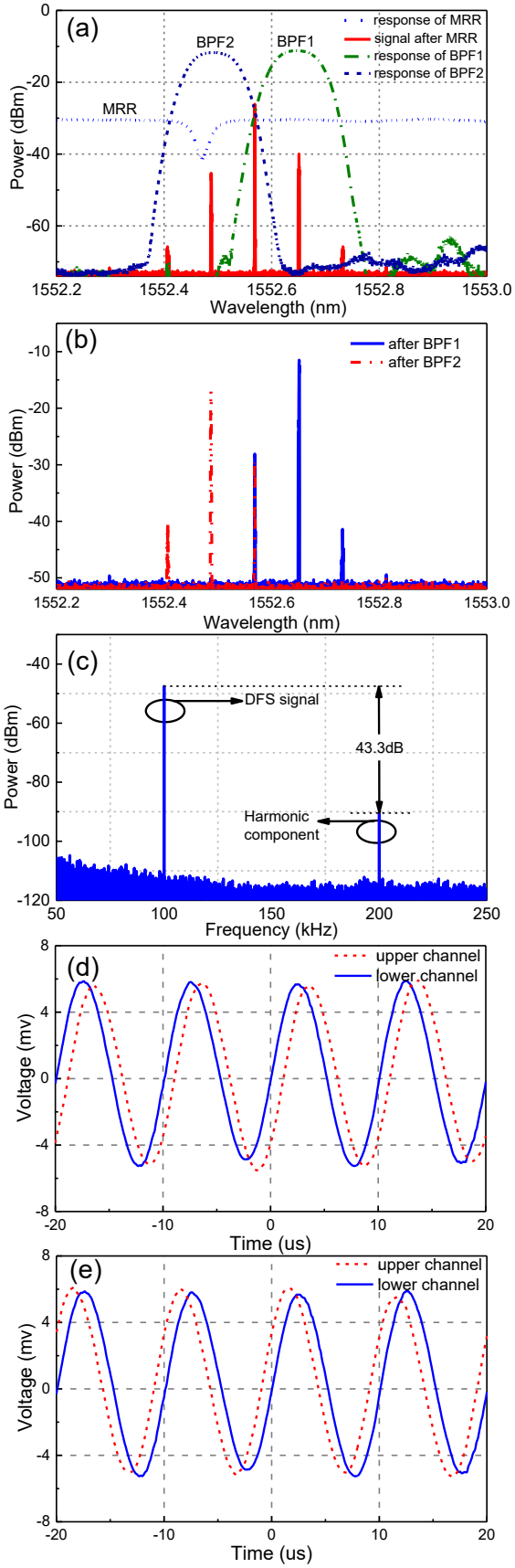

Fig. 4. (a) The measured responses of the MRR, BPFs, and the optical spectra of the output signals. (b) The measured optical spectra after BPFs. (c) The electrical spectrum of the DFS signal. The electrical waveforms of different channels with a (d) negative and (e) positive DFS.

TeraXion Inc.). After being boosted to 22 dBm by an EDFA (Amonics AEDFA-23-B-FA), the optical carrier is coupled into the SOI chip with its polarization state adjusted to be consistent with the grating coupler through a PC. A transmitted signal and an echo signal are produced by two synchronized microwave sources (R&S SMA100B and Keysight MXG N5183B). A voltage-controlled electrical phase shifter with a bandwidth of 8-26.5GHz is applied to emulate the phase difference between the two received signals. The output signal of the chip is amplified by another EDFA (Amonics AEDFA-23-B-FA) and spilt into two channels by a 1×2 optical coupler. The upper and lower sidebands are separately selected by the BPFs (Yenista XTM-50) and injected into low-speed PDs.

In the first step, the powers of the echo and transmitted signals are set as 12 and 10 dBm, respectively, and their frequencies are 10 and 10.0001 GHz. Fig. 4(a) shows the responses of the BPFs and the spectrum of the optical signal after the MRR measured by an optical spectrum analyzer (APEX AP2040D). As can be seen, since the -1st-order sideband falls into the resonance region of the MRR, a phase shift of $\varphi \approx 34^{o}$ is introduced to it, according to the phase response of the MRR shown in Fig. 2(d). Meanwhile, the optical spectra of output signals after the BPFs in two channels are shown in Fig. 4(b). The electrical spectrum of the DFS signal and the harmonic component are obtained by an electrical spectrum analyzer (R&S FSV-40) and shown in Fig. 4(c). The signal-to-noise ratio (SNR) of the DFS measurement is about 43.3 dB and can be further improved by using filters with shaper factors. Figs. 4(d) and 4(e) present the electrical waveforms of the DFS signals in the two channels by a 100 MHz-bandwidth digital oscilloscope (SIGLENT SDS 1102CNL+). Two IF signals with different phase relationships are obtained. According to (5), when the phase of the DFS signal in the lower channel is ahead of the upper one (i.e., Fig. 4(d)), the direction of the DFS is negative, otherwise, the direction of the DFS is positive, as presented in Fig. 4(e).

Fig. 5(a) shows the measured noise floor, 1 dB compression point and compression dynamic range (CDR) of the proposed measurement system. As can been seen, the noise floor of this system is about -145 dBc/Hz. The noise sources mainly include relative intensity (RIN) noise, thermal noise, shot noise and amplifier spontaneous emission (ASE) noise. Thermal noise is a fundamental noise, which is related to the environment temperature. At the room temperature, the thermal noise is about -174 dBc/Hz. Therefore, the noise floor could be expressed as

$$N_{fl} = -174 + NF \tag{7}$$

NF is the noise figure of the system, which can be written as

$$NF = 10\log\left(\frac{s_{in} / n_{in}}{s_{out} / n_{out}}\right) \tag{8}$$

where s_{in} and s_{out} are the intensities of the input and output signals, n_{in} and n_{out} are the intensities of the input and output noises, respectively. Meanwhile, $s_{out}=g_i \cdot s_{in}$ and $n_{out}=g_i \cdot n_{in}+n_{add}$, where g_i is the gain of the link, $n_{add}=n_{th}+n_{RIN}+n_{sh}+n_{ASE}$ is the additional noise of the system. n_{th} is the thermal noise, n_{RIN} is

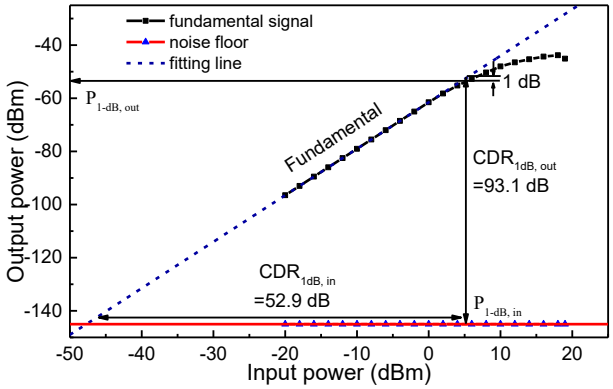

Fig. 5. Measured 1-dB compression point and compression dynamic range of the proposed measurement system.

the relative intensity noise of the laser, n_{sh} is the shot noise of the PD, n_{ASE} is the ASE noise introduced by the EDFA. Therefore, the *NF* could be rewritten as

$$NF = 10\log(1+\frac{n_{th}+n_{RIN}+n_{sh}+n_{ASE}}{g_i n_{th}}) \quad (9)$$

It should be noted that the ASE noise consists of signal-ASE beat noise, ASE-ASE beat noise and shot-ASE beat noise, within which the signal-ASE beat noise is dominated. In the experiment, the noise floor without EDFA is also measured and the value is about -156 dBc/Hz. Therefore, it can be calculated that the noise figure of each EDFA is about 5.5 dB. Besides, as shown in Fig. 5, the input and output 1-dB compression points are 5.12 dBm and -53.1 dBm, respectively. The corresponding input and output CDR_{1dB} of the system are 52.9 dB and 93.1 dB. The sensitivity of the proposed measurement system is also investigated at different carrier frequencies. In this experiment, the power of transmitted signal is set as 10 dBm and the echo signal power is variable. Measurement results show that the sensitivities of the proposed system are about -45, -43 and -39 dBm at carrier frequencies of 10, 15 and 20 GHz, respectively.

To further investigate the tunability and accuracy of the proposed system, the DFS is changed within ±100 kHz at the carrier frequencies of 10, 15 and 20 GHz, which corresponds to the speed ranges of ±3, ±2 and ±1.5 km/s. Meanwhile, to maintain the selected sidebands fall into the resonance region of the MRR, a set of corresponding voltages of 0, 1.2, and 2.3 V are applied to the DC pad. The DFS and velocity measurement results are shown in Fig. 6(a) and Fig. 6(b), respectively. As can be seen, the maximum measurement errors are 0.021, 0.028 and 0.022 Hz, which means that the maximum speed measurement errors are 6.3×10^{-4}, 5.6×10^{-4} and 3.3×10^{-4} m/s at 10, 15 and 20 GHz frequency bands, respectively. An intuitive description of the actual speeds and measurement errors is also depicted in Fig. 6(b). The measurement error is mainly affected by the accuracy of the equipment, this system itself does not bring additional error to the DFS measurement.

In the AOA measurement, performances at the carrier frequencies of 10, 15 and 20 GHz are also demonstrated. A phase difference is introduced between the received signals by a voltage-controlled phase shifter. Fig. 7(a) depicts the measured power of the DFS signal when the phase difference

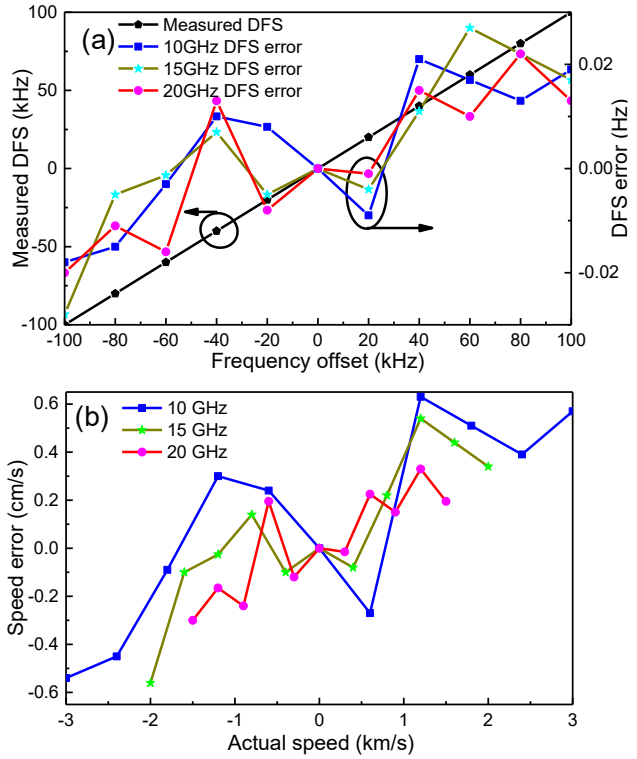

Fig. 6. (a) Measured DFS and error. (b) Measured actual speed and error.

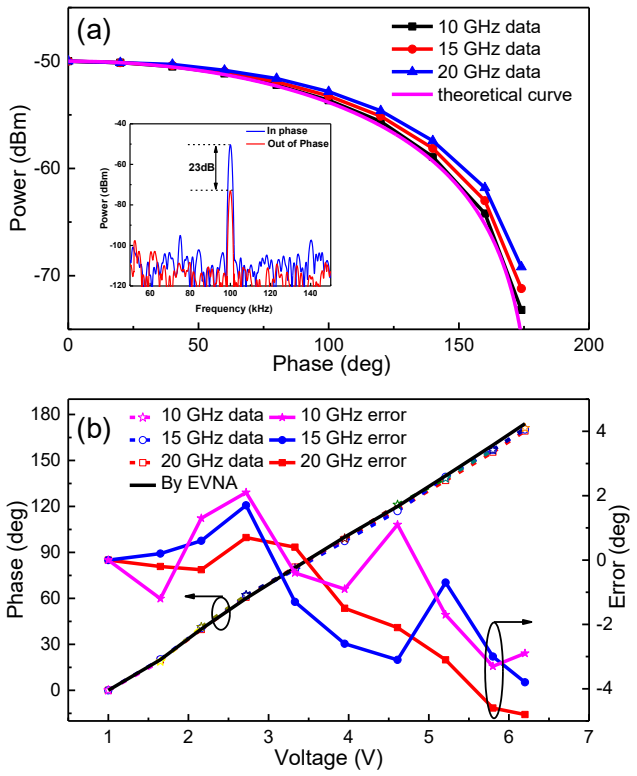

Fig. 7. (a) Measured data scatter and theoretical curve. (b) Phase shifts measured by EVNA and by our method, and the measurement error. Inset in (a): the spectrum of the DFS signal with the maximum and minimum power.

changes in different carrier frequencies. To examine the

accuracy of the AOA measurement system, a theoretical curve based on (6) is also plotted in Fig. 7(a). The available measurement range of phase difference is about 174°. The inset in Fig. 7(a) shows the power variation range (~23 dB) of the DFS signal at the carrier frequency of 10 GHz, which corresponds to the variation range of the phase difference between the echo signals. Additionally, an electrical vector network analyzer is also used to measure the phase shifts and the result is shown in Fig. 7(b). When comparing with the results obtained by the proposed AOA measurement system, the maximum errors between the two different measurement methods are about 3.3°, 3.8° and 4.8° at the carrier frequencies of 10, 15 and 20 GHz, respectively. According to the relationship between AOA and the phase difference (i. e., ψ=arcsin(θ/π)), the measurement range of AOA is about from 0° to 75°, and the maximum measurement error is about 1.05°, 1.21° and 1.53° at 10, 15 and 20 GHz frequency bands, respectively.

V. Discussion

In order to verify the system stability, the DFS measurement within 60 minutes is carried out. The frequency fluctuation of the measured DFS, as shown in Fig. 8, is kept within ±0.002 Hz, which demonstrates the good system stability for DFS measurement. For the AOA measurement, since only the sidebands out of the resonance are used, the influence of temperature drift occurred on the MRR could be neglected. However, since a temperature controller is not available in our lab, the long-term stability of the MRR is not good enough, which may affect the long-term performance of the system. In a practical application, a temperature controller is necessary to ensure the stability of the MRR.

It is worth noting that the operating carrier frequency of our system is only limited by the bandwidth of the modulators and the optical filters. According to the measured parameters of the modulators and BPFs, the carrier frequency range of this system is about 5-21.4GHz for both the DFS and AOA measurement. Moreover, as can be seen from the results shown in Fig. 6 and Fig. 7, since the DFS error is mainly affected by the accuracy of the equipment, the measured DFS error is independent to the carrier frequency. The AOA measurement error is slightly larger as the increase of the carrier frequency, which may owe to the relatively poorer performances of the electro-optic devices at the higher frequency band.

Although in our chip, only two DDMZMs and an MRR are integrated on an SOI chip, according to the current level of integration technology, the out-of-chip devices, including the 1550-nm band laser [39], optical amplifier [40], BPF [41] and PD [41], could also be integrated with good performance, which means that this system could be monolithically integrated on a single chip.

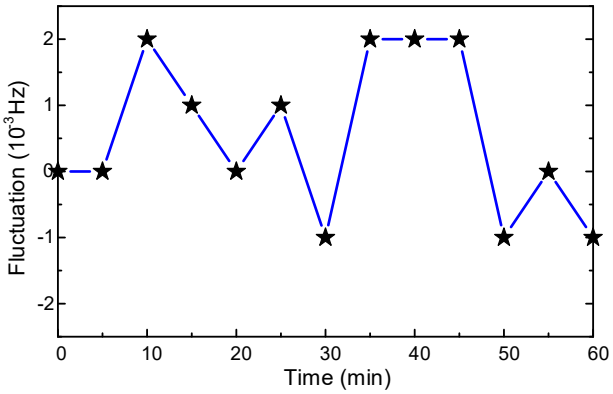

Fig. 8. Fluctuation of the DFS within 60 minutes.

In our experiment, the demonstrated phase difference measurement range is 174° (i. e., the maximum AOA is ~75 °). According to Eq. (6), the phase difference is mapped to the power of the output electrical signal, so the maximum value of the phase difference measurement is determined by the minimum power at the output of the PD. In principle, when the phase difference is 180° (i. e., AOA is 90°), the ±1st sidebands generated by DDMZM1 will be out of phase. In this condition, they can be completely canceled, and no microwave signal will be obtained at the output of the PD. However, due to the asymmetrical characteristics of the sub-phase shifters in the two arms of DDMZM1, residual sidebands will be existed at the output of DDMZM1. When the residual sidebands are beaten with the sidebands generated by DDMZM2, an unwanted IF signal will still be produced. As a result, to increase the AOA measurement range, a DDMZM with an improved symmetrical performance is desired.

In order to directly show the advantages and disadvantages of the proposed method, a comparison with previous works in terms of size, function, cost, complexity, carrier frequency range and measurement error is also listed in Table I. As can be seen, the proposed system increases the degree of integration and achieves DFS and AOA measurements simultaneously.

VI. Conclusion

In this paper, we have proposed and experimental demonstrated a photonic-chip-based DFS and AOA measurement system. At the carrier frequencies of 10, 15, and 20 GHz, the maximum DFS error within ±100 kHz is less than ±0.021, ±0.028 and ±0.022 Hz and the AOA measurement error within 0-75° is less than ±1.05°, ±1.21° and ±1.53°. To the best of our knowledge, this is the first DFS and AOA measurement system based on a silicon integrated circuit, which provides a feasible way towards the high-performance monolithic integration of the AOA and DFS measurement system.

TABLE I
A Comparison of Previous Works and This Work

Size	Function	Cost	Complexity	Measurement range	Carrier frequency	Measurement error	Ref.
Discrete device	AOA	High	Simple	0°-65°	2.65-12.62 GHz	<1.9°	[11]

Discrete device	AOA	Low	Simple	-160°-40°	18 GHz	<2.5°	[12]
Discrete device	AOA	Low	Simple	5°-165°	12.5 GHz	<3.1°	[13]
Discrete device	AOA	Low	Simple	0°-165°	15 GHz	<2.24°	[14]
Discrete device	AOA	Low	Simple	0°-76.8°	10-15 GHz	<2°	[15]
Discrete device	AOA	Low	Complex	18.22°-90°	5 GHz	<1°	[16]
Discrete device	AOA	High	Complex	0°-90°	10-18 GHz	<4.5°	[17]
Discrete device	DFS	Low	Complex	±100 kHz	10-39 GHz	$<\pm5\times10^{-6}$ Hz	[18]
Discrete device	DFS	Low	Complex	±1 MHz	10-14 GHz	≈0	[19]
Discrete device	DFS	High	Complex	±100 kHz	5-40 GHz	<±12 Hz	[20]
Discrete device	DFS	High	Complex	±90 kHz	10-38 GHz	<±5.8 Hz	[21]
Discrete device	DFS	High	Complex	±100 kHz	10-18 GHz	$<\pm5\times10^{-6}$ Hz	[22]
Discrete device	DFS	Low	Complex	±90 kHz	10-20 GHz	<±60 Hz	[23]
Discrete device	DFS	Low	Simple	10-100 kHz	15-30 GHz	$<\pm5\times10^{-10}$ Hz	[24]
Discrete device	DFS	Low	Complex	0-456 kHz	10-40 GHz	<1.5% at 0 dBm	[30]-[32]
Discrete device	AOA&DFS	Low	Complex	1.82°-90°/±100 kHz	20 GHz	$<0.85°/<\pm5\times10^{-3}$ Hz	[33]
Discrete device	AOA&DFS	High	Complex	0°-90°/±300 kHz	15 GHz	<±1°/<±0.2 Hz	[34]
Discrete device	AOA&DFS	Low	Complex	0°-90°/±100 kHz	20 GHz	<1.3°/<±0.08 Hz	[35]
Partial integration	DFS	High	Simple	±100 kHz	10 GHz	<1 Hz	[37]
Partial integration	AOA&DFS	Low	Complex	0°-75°/±100 kHz	5-21.4 GHz	<1.53°/<±0.028 Hz	This work

REFERENCES

[1] A. E. Spezio, "Electronic warfare systems," *IEEE Trans. Microw. Theory Techn.*, vol. 50, no. 3, pp. 633-644, Aug. 2002.

[2] Z. Tang and S. Pan, "Simultaneous measurement of Doppler-frequency-shift and angle-of-arrival of microwave signals for automotive radars," in *Proc. Int. Topical Meeting Microw. Photon*., 2019, pp. 1–4.

[3] V. C. Chen, F. Li, S.-S. Ho, and H. Wechsler, "Micro-Doppler effect in radar: phenomenon, model, and simulation study," *IEEE Trans. Aerosp. Electron. Syst.*, vol. 42, no. 1, pp. 2-21, Jan. 2006.

[4] S. Pan and Y. Zhang, "Microwave photonic radars," *J. Lightwave Technol.*, vol. 38, no. 19, pp. 5450-5484, Oct. 2020.

[5] S. Pan, X. Ye, Y. Zhang, and F. Zhang, "Microwave photonic array radars," *IEEE J. Microwaves*. vol. 1, no. 1, pp. 176-190, Jan. 2021.

[6] S. Pan and J. Yao, "Photonics-based broadband microwave measurement," *J. Lightwave Technol.*, vol. 35, no. 16, pp. 3498-3513, Aug. 2017.

[7] X. Zou, B. Lu, W. Pan, L. Yan, A. Stöhr, and J. Yao, "Photonics for microwave measurements," *Laser & Photonics Reviews*. vol. 10, no. 5, pp. 711-734, Sep. 2016.

[8] J. P. Yao, "Microwave photonics", *J. Lightw. Technol.*, vol. 27, no. 1–4, pp. 314-335, Jan. 2009.

[9] B. Vidal, M. Á. Piqueras, and J. Martí, "Direction-of-arrival estimation of broadband microwave signals in phased-array antennas using photonic techniques," vol. 24, no. 7, pp. 2741, Mar. 2006.

[10] Z. Tu, A. Wen, Z. Xiu, W. Zhang, and M. Chen, "Angle-of-arrival estimation of broadband microwave signals based on microwave photonic filtering," *IEEE Photon. J.*, vol. 9, no. 5, pp. 1-8, Oct. 2017.

[11] H. Chen and E. H. W. Chan, "Angle-of-arrival measurement system using double RF modulation technique," *IEEE Photon. J.*, vol. 11, no. 1, pp. 1-10, Feb. 2019.

[12] X. Zou, W. Li, W. Pan, B. Luo, L. Yan, and J. Yao, "Photonic approach to the measurement of time-difference-of-arrival and angle-of-arrival of a microwave signal," *Opt. Lett.*, vol. 37, no. 4, pp. 755-757, Feb. 2012.

[13] Z. Cao, Q. Wang, R. Lu, H. P. van den Boom, E. Tangdiongga, and A. M. Koonen, "Phase modulation parallel optical delay detector for microwave angle-of-arrival measurement with accuracy monitored," *Opt. Lett.*, vol. 39, no. 6, pp. 1497-1500, Mar. 2014.

[14] H. Zhuo, A. Wen, and Y. Wang, "Photonic angle-of-arrival measurement without direction ambiguity based on a dual-parallel Mach–Zehnder modulator," *Opt. Commun.*, vol. 451, pp. 286-289, Nov. 2019.

[15] H. Chen and E. H. Chan, "Simple approach to measure angle of arrival of a microwave signal," *IEEE Photon. Technol. Lett.*, vol. 31, no. 22, pp. 1795-1798, Oct. 2019.

[16] Z. Zhang, Y. Wang, Z. Zhu, S. Zhao, J. Liu, W. Jiang, and G. Wu, "Photonic 2-D angle-of-arrival estimation based on an L-shaped antenna array for an early radar warning receiver," *Opt Express*. vol. 28, no. 26, pp. 38960-38972, Dec. 2020.

[17] P. Li, L. Yan, J. Ye, X. Feng, X. Zou, B. Luo, W. Pan, T. Zhou, and Z. Chen, "Angle-of-arrival estimation of microwave signals based on optical phase scanning," *J. Lightwave Technol.*, vol. 37, no. 24, pp. 6048-6053, Dec. 2019.

[18] W. Chen, A. Wen, X. Li, Y. Gao, Y. Wang, S. Xiang, H. He, and H. Zheng, "Wideband Doppler frequency shift measurement and direction discrimination based on a DPMZM," *IEEE Photon. J.*, vol. 9, no. 2, pp. 1-8, Apr. 2017.

[19] C. Yi, H. Chi, and T. Jin, "A photonic approach for doppler frequency shift measurement with dispersion medium," *IEEE Photon. J.*, vol. 12, no. 5, pp. 1-8, Oct. 2020.

[20] F. Zhang, J. Shi, and S. Pan, "Photonics-based wideband Doppler frequency shift measurement by in-phase and quadrature detection," *Electron. Lett.*, vol. 54, no. 11, pp. 708-710, May 2018.

[21] B. Lu, W. Pan, X. Zou, Y. Pan, X. Liu, L. Yan, and B. Luo, "Wideband microwave Doppler frequency shift measurement and direction discrimination using photonic I/Q detection," *J. Lightwave Technol.*, vol. 34, no. 20, pp. 4639-4645, Jun. 2016.

[22] X. Li, A. Wen, W. Chen, Y. Gao, S. Xiang, H. Zhang, and X. Ma, "Photonic Doppler frequency shift measurement based on a dual-polarization modulator," *Appl. Opt.*, vol. 56, no. 8, pp. 2084-2089, Mar. 2017.

[23] B. Lu, W. Pan, X. Zou, X. Yan, L. Yan, and B. Luo, "Wideband Doppler frequency shift measurement and direction ambiguity resolution using optical frequency shift and optical heterodyning," *Opt. Lett.*, vol. 40, no. 10, pp. 2321-2324, May 2015.

[24] X. Zou, W. Li, B. Lu, W. Pan, L. Yan, and L. Shao, "Photonic approach to wide-frequency-range high-resolution microwave/millimeter-wave Doppler frequency shift estimation," *IEEE Trans. Microw. Theory Techn.*, vol. 63, no. 4, pp. 1421-1430, Apr. 2015.

[25] C. Yi, H. Chi, B. Yang, and T. Jin, "A PM-based approach for Doppler frequency shift measurement and direction discrimination," *Opt. Commun.*, vol. 458, pp. 124796, Mar. 2020.

[26] L. Xu, Y. Yu, H. Tang, and X. Zhang, "A simplified photonic approach to measuring the microwave Doppler frequency shift," *IEEE Photon. Technol. Lett.*, vol. 30, no. 3, pp. 246-249, Dec. 2017.

[27] J. Li, W. Yu, Z. Zhang, T. Lin, S. Dai, and J. Liu, "Simple approach for Doppler frequency shift estimation based on a dual-polarization quadrature phase shift keying (DP-QPSK) modulator," *Appl. Opt.*, vol. 59, no. 7, pp. 2114-2120, Mar. 2020.

[28] P. Zuo and Y. Chen, "Photonic-assisted filter-free microwave Doppler frequency shift measurement using a fixed low-frequency reference signal," *J. Lightwave Technol.*, vol. 38, no. 16, pp. 4333-4340, Aug. 2020.

[29] Y. Chen, P. Zuo, T. Shi, and Y. Chen, "Photonic-enabled Doppler frequency shift measurement for weak echo signals based on optical single-sideband mixing using a fixed low-frequency reference," *J. Lightwave Technol.*, vol. 39, no. 10, pp. 3121-3129, Feb. 2021.

[30] H. Emami, M. Hajihashemi, S. E. Alavi, and M. Ghanbarisabagh, "Simultaneous Echo Power and Doppler Frequency Measurement System

Based on Microwave Photonics Technology," *IEEE Trans. Instrum. Meas*., vol. 66, no. 3, pp. 508-513, Jul. 2017.
[31] H. Emami, M. Hajihashemi, and S. E. Alavi, "Standalone Microwave Photonics Doppler Shift Estimation System," *J. Lightwave Technol.*, vol. 34, no. 15, pp. 3596-3602, Jun. 2016.
[32] H. Emami, M. Hajihashemi, and S. E. Alavi, "Improved Sensitivity RF Photonics Doppler Frequency Measurement System," *IEEE Photon. J.*, vol. 8, no. 5, pp. 1-8, Aug. 2016.
[33] P. Li, L. Yan, J. Ye, X. Feng, W. Pan, B. Luo, X. Zou, T. Zhou, and Z. Chen, "Photonic approach for simultaneous measurements of Doppler-frequency-shift and angle-of-arrival of microwave signals," *Opt Express*. vol. 27, no. 6, pp. 8709-8716, Mar. 2019.
[34] C. Huang, H. Chen, and E. H. W. Chan, "Simple photonics-based system for Doppler frequency shift and angle of arrival measurement," *Opt Express*. vol. 28, no. 9, pp. 14028-14037, Apr. 2020.
[35] J. Zhao, Z. Tang, and S. Pan, "Photonic approach for simultaneous measurement of microwave DFS and AOA," *Appl. Opt.*, vol. 60, no. 16, pp. 4622-4626, Jun. 2021.
[36] H. Zhuo and A. Wen, "A Photonic approach for doppler-frequency-shift and angle-of-arrival measurement without direction ambiguity," *J. Lightwave Technol.*, vol. 39, no. 6, pp. 1688-1695, Dec. 2021.
[37] Z. Cui, Z. Tang, S. Li, Z. He, and S. Pan, "On-chip photonic method for Doppler frequency shift measurement," in *Proc. Int. Topical Meeting Microw. Photon*., 2019, pp. 1–3.
[38] M. I. Skolnik, *Radar Handbook*, 3rd ed. New York, NY, USA: McGraw-Hill, 2008.
[39] Y. Qin, S. Ding, M. Zhang, Y. Wang, Q. Shi, Z. Li, J. Wen, M. Xiao, and X. Jiang, "High-power, low-noise Brillouin laser on a silicon chip," *Opt. Lett*., vol. 47, no. 7, pp. 1638-1641, Apr. 2022.
[40] T. Matsumoto, T. Kurahashi, R. Konoike, K. Suzuki, K. Tanizawa, A. Uetake, K. Takabayashi, K. Ikeda, H. Kawashima, S. Akiyama, and S. Sekiguchi, "Hybrid-Integration of SOA on Silicon Photonics Platform Based on Flip-Chip Bonding," *J. Lightwave Technol.*, vol. 37, no. 2, pp. 307-313, Feb. 2019.
[41] Y. Ding, M. Pu, L. Liu, J. Xu, C. Peucheret, X. Zhang, D. Huang, and H. Ou, "Bandwidth and wavelength-tunable optical bandpass filter based on silicon microring-MZI structure," *Opt. Express*. vol. 19, no. 7, pp. 6462-6470, Mar. 2011.
[42] K. Sun, D. Jung, C. Shang, A. Liu, J. Morgan, J. Zang, Q. Li, J. Klamkin, J. E. Bowers, and A. Beling, "Low dark current III-V on silicon photodiodes by heteroepitaxy," *Opt Express*. vol. 26, no. 10, pp. 13605-13613, May 2018.

Liangzun Tang received a B.S. degree from the College of Science, Nanjing University of Aeronautics and Astronautics, Nanjing, China, in 2014, where he is currently working toward the Ph.D. degree. His research interests include photonic microwave generation and measurement, optoelectronic oscillator, and integrated microwave photonics.

Zhenzhou Tang (Member, IEEE) received the M.S. degree in information engineering from the Nanjing University of Aeronautics and Astronautics, Nanjing, China, in 2014 and double Ph.D. degrees in Communication and Information System from Nanjing University of Aeronautics and Astronautics (NUAA) and in Photonics Engineering from Ghent University (UGent), Belgium, in 2019 and 2020, respectively. He is currently an Associate Professor with the Key Laboratory of Radar Imaging and Microwave Photonics, Ministry of Education, NUAA. He has authored or coauthored more than 40 research papers, including more than 15 papers in peer-reviewed journals and 15 papers in conference proceedings. His research interests include photonics-based microwave mixing, photonic integrated circuits, and radio over fiber communications. He is one of the recipients of the 2017 IEEE Photonics Society Graduate Student Fellowship. He is also the affiliated member of IEEE MTT-S Microwave Photonics Committee.

Siming Li received the B.S. and Ph.D. degrees from Nanjing University, Nanjing, China, in 2009 and 2014, respectively. In 2014, she joined the Key Laboratory of Radar Imaging and Microwave Photonics, Ministry of Education, where she is currently an associate professor. Her current research focuses on integrated microwave photonic device and system.

Shifeng Liu received the B.S. and M.S. degrees in electronics engineering from Nanjing University of Aeronautics and Astronautics, Nanjing, China, in 2012 and 2015, respectively. He is currently working toward the P.H.D degree at the Key Laboratory of Radar Imaging and Microwave Photonics (Nanjing Univ. Aeronaut. Astronaut.), Ministry of Education. He has authored or coauthored more than 18 papers in peer-reviewed journals and 5 papers in conference proceedings. His research interests include ultra-low phase noise photonic-microwave generation, microwave photonic measurement, and radio over fiber systems.

Shilong Pan (Senior Member, IEEE) received the B.S. and Ph.D. degrees in electronic engineering from Tsinghua University, Beijing, China, in 2004 and 2008, respectively. From 2008 to 2010, he was a “Vision 2010” Postdoctoral Research Fellow in the Microwave Photonics Research Laboratory, University of Ottawa, Canada. He joined the College of Electronic and Information Engineering, Nanjing University of Aeronautics and Astronautics, China, in 2010, where he is currently a Full Professor and an Executive Director of the Key Laboratory of Radar Imaging and Microwave Photonics, the Ministry of Education. His research has focused on microwave photonics, which includes optical generation and processing of microwave signals, analog photonic links, photonic microwave measurement, and integrated microwave photonics. Prof. Pan has authored or co-authored over more than 400 papers in peer-reviewed journals and conference proceedings. Prof. Pan is currently an associate editor of Journal of Lightwave Technology, Electronics Letters, and PhotoniX, and a deputy editor of Chinese Optics Letters. He is the vice chair of IEEE MTT-22 Microwave Photonics. Prof. Pan has also served as a Chair of a number of international conferences, symposia, and workshops, including the TPC Chair of ICOCN 2015, TPC Co-chair of IEEE MWP 2017, and the General Co-chair of IEEE MWP 2021. Prof. Pan is a Fellow of OSA, SPIE and IET. He was selected as an IEEE Photonics Society Distinguished Lecturer in 2019 and was a recipient of IEEE MTT-S Outstanding Young Engineer Award in 2021.